Investigation of cavitation and air entrainment during pilot injection in real-size multi-hole diesel nozzles

Eduardo Gomez Santos[a,c], Junmei Shi[a,*], Manolis Gavaises[c], Celia Soteriou[b], Mark Winterbourn[b], Wolfgang Bauer[d]

[a] *Delphi Technologies, Avenue de Luxembourg, 4940 Bascharage, Luxembourg*
[b] *Delphi Technologies, Courteney Rd, Gillingham ME8 0RU, UK*
[c] *City, University of London, Northampton Square, London EC1V 0HB, UK*
[d] *ANSYS Germany GmbH, Staudenfeldweg 20, 83624 Otterfing, Germany*

Abstract

This paper investigates the complex multiphase flow developing inside the micro-orifices of diesel injector nozzles during pilot injection. High speed micro-visualisations of a transparent serial production nozzle tip replica are used to record the multiphase flow inside the flow orifices as well as near-nozzle spray development. The physical processes taking place are explained with the aid of a three-phase (liquid, vapour and air) homogeneous mixture model utilized in the context of Large Eddy Simulations. Phase-change due to cavitation is considered with a model based on the Rayleigh-Plesset equation, while compressibility of all the phases is accounted for. Numerical simulations shed light on the interaction between the vortex flow and cavitation formation that take place simultaneously with air entrainment from the surrounding environment into the injector's sac volume during the injec-

*Corresponding author
Email address: junmei.shi@delphi.com (Junmei Shi)

tion and the dwell time between successive injections. The experimentally observed flow phenomena are well captured by the simulation model. In particular the compression of pre-existing air bubbles inside the injector's sac volume during the injector opening, cavitation vapor condensation and air suction after the needle closure are well reproduced.
Keywords: LES, Multiphase flow, Cavitation, Fuel Injection, Pilot injection, Air entrainment

1. Introduction

New European Real Driving Emission (RDE) driving cycle legislations require significant research efforts to develop emission compliant and efficient passenger car engines [1]. In this context, the so-called digital injection schemes, used to split the fuel injection into multiple small injections with close separation among them, are widely applied in modern diesel engines in order to obtain simultaneous reductions in noise and emissions without compromising engine performance and fuel consumption [2, 3].Although the nozzle flow for static needle lift conditions has been extensively investigated (see selectively [4, 5, 6, 7]), not much work is available for the flow development during the dynamic operation of the injector, which plays a key influence on emissions [8, 9].

The digital injection schemes are often operated with fast injector needle opening and closing and with very small separation between injections; with typical dwell time of the order of $50\mu s$. This results in highly transient flow

Nomenclature

α_{air}	air volume fraction	[-]
α_{liq}	liquid fuel volume fraction	[-]
α_{nuc}	nuclei content	[-]
α_{vap}	vapor fuel volume fraction	[-]
$\boldsymbol{v}$	velocity field	[m/s]
λ_g	Taylor length scale	[m]
μ	viscosity	[Pa s]
μ_t	turbulent viscosity	[Pa s]
ρ	density	$[kg/m^3]$
ρ_{vap},ρ_{air}	vapour/air density	$[kg/m^3]$
σ	viscous stress tensor	[Pa]
τ_t	turbulent stresses	[Pa]
D	injection hole diameter	[m]
E	total energy	[J/kg]
F_{vap}, F_{cond}	empirical constants	$[m^{-1}]$
p	pressure field	[Pa]
R	gas constant	[J/kg/K]
R_b	bubble radius	[m]
R_e, R_c	evaporation/condensation rate	$[kg/m^3/s]$
Re	Reynolds number	[-]
T	temperature	[K]
y^+	non-dimensional wall disatance	[-]

and formation of cavitation inside the injection nozzle. In addition, modern diesel engines are operated under high injection pressure ($> 2500bar$) and utilise injectors with small injection hole diameters ($90 - 120\mu m$); these conditions pose significant difficulties in measuring and/or optically visualising the processes occurring in both the injector nozzle and within the high temperature combustion chamber. The majority of transparent real-size nozzle investigations featuring simplified single-hole geometries that generally confirm the presence of geometric-induced cavitation [10, 11, 12]. The work of [13, 14, 15], and the relevant early modelling work [16] were the first to substitute one of the holes of a production nozzle with a quartz window of identical geometric characteristics and was an experimental breakthrough that provided valuable information on flow and cavitation structures inside such micro-channels under realistic operating conditions; further studies were reported in [17]. A step forward was realised in [18], where a 3-hole, real-size, fully transparent nozzle allowed for unobstructed optical access inside the sac volume. Vortex cavitation is dramatically enhanced by vapour or air already present inside the nozzle volume [19]. Moreover, [20] showed that the structure of a vortex core is significantly affected by entrained vapour bubbles. Similarly, [21] demonstrated possible fragmentation of the vortex core so as to increase the vorticity at the core centre. Finally, the strong interaction observed between vortex properties and bubble dynamics[22], the coupling of radial and axial growth of bubbles trapped in vortices [23] and the interaction between shear (or normal strain) flow and bubble volume change [24] form a tremendously complex flow field inside an injector nozzle, where dynamic changes in the behaviour of vortices and vapour bubbles strongly affect the emerging fuel spray. Highly transient flow phenomena caused by the fast needle response times, give rise to formation of vortical structures and therefore, to string cavitation [25]. Transient effects have also been correlated to increased probability of surface erosion damage, which is attributed to both, geometric and string cavitation [26]. Cavitation in simplified nozzle replicas has been visualized even at pressures as high as $2000bar$, as shown in [27, 28]. Remarkably, in very recent studies, sonoluminescence from cavitation collapse observed in a simplified nozzle replica has been observed for the first time[29] and a neutron imaging technique has been developed overcoming the disadvantages of using materials transparent to visible light[30]. All aforementioned studies report data from one or just a few injection events. The group of the authors has reported in [31, 32, 33]] for the first time averaged images of cavitation developing in a real-size 6-hole transparent tip nozzle for single and pilot-main split injections up to $400bar$. Data from these investigations are further reported here and utilized for validation of the newly developed model. Only the very recent work of [34] has extended the range of operating conditions (injection pressures up to $1000bar$ and back pressures up to $30bar$) and geometrical features studied (hydro erosively ground inlet orifice) for long injections. These studies provide qualitative data on cavitation and air-entrainment inside the fuel injector during the opening and closing of the injector's needle valve. A drawback of the images is that one cannot distinguish between cavitation and air, as they both appear as an indistinguishable black shadow in the obtained images.

Given the limited quantitative information around the flow structure inside diesel injectors, fuel injection equipment manufacturers require robust predictive Computational Fluid Dynamics (CFD) tools, in order to understand the physical mechanisms taking place during injection. From a physical viewpoint, modelling of such flow conditions requires the fluid compressibility [35], mass transfer (cavitation, flash boiling, evaporation etc.) and heat transfer [36, 37, 38] to be taken into account, which increase the complexity as well as the computational cost of the simulations. Additionally, the fluid dynamics processes occur at high Reynolds number and therefore accounting for the effect of turbulence structures and vortex dynamics, is key in explaining how the injected fuel spray is formed [39, 40, 41, 42]; this can only be resolved using very fine computational grids and scale resolving simulations, such as Large Eddy Simulation (LES).

Recent LES including dynamic needle movement for the in-nozzle flow includes the work of Battistoni et al. [43] who simulated the start and end of injection for a single hole nozzle using the cut cell cartesian method for modelling the boundary movement and a homogeneous relaxation model for cavitation phenomena. The work concludes that URANS predictions for the residual liquid back flow occur without fragmentation, while in LES liquid breaks up generating complex three dimensional structures. The URANS approach predicted at the end of the injection an annular void region stemming from the needle seat, which then re-condenses as the pressure is recovered. This was not observed in LES, where regions of low pressure are produced even in areas detached from the needle seat. The predicted near spray region was also different as no ligaments were formed in URANS; instead diffusion disperses the liquid in the surrounding air even if integral values like sac pressure and liquid volume fraction were not greatly affected. Ligament formation and gas ingestion into the nozzle at the end of injection are predicted, as observed experimentally in Phase Contrast X-ray images (for additional

Phase Contrast X-ray studies see for example [9, 44]). The start-of-injection simulation shows how gas is ejected first, and liquid fuel starts being injected with a delay. The main result of these analyses is that if the sac volume is initially filled with gas, the liquid exit is delayed several tens of μs after the start of needle movement, which is in good agreement with the experimental evidence. This delay is of the order of $100\mu s$, and it is compatible with the duration of the first slow rising part of the needle movement. Orley et al. [45] used the cut cell cartesian method to simulate with implicit LES, a barotropic homogeneous equilibrium model for cavitation and a fully compressible 3-phase flow model a complete 9-hole diesel injector. The focus of the work was on the vortical development of the flow and the assessment of erosion sensitive areas during the operation of the injector. After the injector closing, strong collapse events of vapor structures in the needle seat and the sac hole cause the formation of violent shock waves. The authors highlighted that a fully compressible description of the flow is essential to capture such phenomena. It was also concluded that despite steady needle simulations capturing the main flow features reasonably well, vapor creation during the closing phase of the needle valve requires information on the previously developed flow; thus, reliable prediction of erosion-sensitive areas due to collapse events during and after the closing of the needle can only be predicted accurately by including the unsteady needle motion. Finally, the work of Koukouvinis et al. [35] used a 2-phase dynamic needle approach based on a combination of layering and stretching algorithms together with a Rayleigh-Plesset based cavitation model with increased mass transfer, to compute the opening phase of two different injector designs; the findings have correlated the pressure peaks in the domain with areas that suffer from erosion. Whichever the chosen modelling approach may have been, previous studies have lacked validation [45], had indirect validation [35] or were not of direct relevance to modern applications [43], since a single hole nozzle lacks the complex sac recirculation flow present in modern diesel injectors.

On the broader perspective, reduction of exhaust gas and in the same time noise emissions from engines, relies on multiple injection strategies, such as digital rate shaping (DRS) [46, 47, 48, 49], which allow the use of a variety of options for pilot, main, and post-(main) injection events in order to provide a degree of control over the timing and phasing of the ignition delay and heat release events, as reported in [50]. Recent investigations from the group of the authors suggest that when the dwell-period is shortened, there is significant reduction in soot while exhaust-out NOx is controlled by EGR. Similarly, the CN-soot trade-off can be decoupled by reducing pilot-main dwell time, adding a greater number of pilots and increasing rail pressure without compromising fuel consumption [51]. The use of such complex strategies described relies on the ability of the fuel injection equipment to accurately meter extremely small quantities of fuel per event (which may be of the order of $1mg$ of fuel being injected in a period of less than $0.25ms$) over the engine lifetime [49]. During these short metering events the injector will not reach full lift and will be operating within the transient part of the rate curve. To meet these demands, it is extremely important to avoid the accumulation of excessive carbonaceous deposits on, and within the fuel injector. Nozzle hole deposits can reduce the effective flow area of the fuel or cause it to be mis-directed. These effects give rise to poorer atomisation and mixing, excessive spray penetration, and increased risk of fuel impacting on the combustion chamber surfaces, with the potential to adversely affect emissions. The impact of deposit formation within nozzle holes and their effect on engine performance are well summarised in [52], concluding that residual fuel remaining within the injector nozzle's sac and holes are thought to be instrumental in the process [9]. With increasing number of pilot injections with short dwell time, the residual fuel in the nozzle sac after needle closure can be critical for the HC and soot emissions. However, experimentation of the detailed flow dynamics inside the injector at such conditions is practically impossible; currently there is no study reporting quantitative data on the flow development during the injection events for such processes. The experimental data reported in [31, 32, 33, 34] clearly indicate that the flow and cavitation development inside the injector is different in every injection cycle, and differ significantly from the experimentally derived time-averaged field, as shown in [32]. An alternative to shed light to those processes, is the use of computational fluid dynamics. The current work, to the best of the authors knowledge, presents for the first time application of a 3-phase LES to the flow in a diesel injector for a pilot injection event, including cavitation and compressibility of all phases; simulations have utilised the optically measured needle valve movement from fully transparent real size 6-hole nozzle tips [31, 32, 33], as reported by the group of the authors. Moreover, the high-speed shadowgraph images from those studies serve as validation of the developed model; these include the location/timing of cavitation initiation, its further extent and eventual collapse and the air entering into the injection holes and sac volume of the nozzle tip.

The need to employ LES derives from the necessity to predict the flow formation of individual injection cycles, as opposed to cycle-averaged flow distribution. The complexity of the flow is not only linked to the formation of cavitation, but also to the residual air present inside the injector; this has been considered in the present work by initialising the residual air distribution inside the injector's sac volume and injection holes from the images recorded for individual injection events. Moreover, inclusion of compressibility effects for all phases is deemed as necessary for resolving the complex liquid, cavitation formation and development and air compression/expansion inside the injector, as it is shown in the reported results.

The present paper is structured in the following way: first an overview on the experimental results is given for a diesel pilot injection visualization of a transparent nozzle tip. Then the numerical methodology employed is described in detail, followed by the comparison of the CFD results with the transparent nozzle visualisations for which good agreement is obtained and interpretation of the observed phenomena is provided.

2. Experimentally observed multiphase phenomena

As already mentioned, the 3-phase simulation methodology has been validated against high speed visualisations of a transparent Delphi Technologies Diesel 6-hole nozzle tip manufactured by City, University of London. The metallic injector nozzle tip was substituted with a transparent acrylic tip. The design is a standard serial production geometry, i.e not just a multi-hole nozzle, but a fully operational, serial production type. The detailed results and findings of that experimental campaign as well as the setup details were reported in [31, 32, 33] and will not be repeated here. The 6-hole transparent tip has holes with no taper (zero conicity) and a nominal diameter (D) of $160\mu m$. The electrical pulse activation width for a pilot injection was $0.5ms$. High speed cameras recorded the events at a frame rate of $30000fps$. An example of a pilot injection for a rail pressure of 300bar into atmospheric conditions can be found in Figure 1. Given the image acquisition rate, the pilot injection including all major events after closing lasts for 24 frames. As discussed in [32, 33] air trapped in the sac after the end of the injection aggregates forming bubbles in the sac and occupying part of the hole. Prior to $233.33\mu s$ after the electrical trigger, no change is observed and therefore images are not shown. Then the trapped bubble shows slight expansion due to the initial volume created by the needle as it starts lifting ($300\mu s$ after the trigger) and subsequent compression ($400\mu s$ after the trigger) highlighting the need to model air compressibility. This is followed by void coming from the seat passage and its advection into the hole ($500\mu s$ after the trigger).

Then, due to flow acceleration at the hole entrance, void structures are seen in the hole during the opening phase ($600\mu s$ after the trigger). During the needle closing phase, vapour increases substantially in the hole and void coming from the seat reappears ($633.33\mu s$ after trigger). At the end of the injection, the sac gets full with bubbles and the spray greatly weakens ($733.33\mu s$ after the trigger), followed by what seems to be air suction ($766.66\mu s$ after the trigger). Finally, a bubbly mixture is observed floating in the sac as well as an oscillatory movement of the air in the hole ($1000\mu s$ after the trigger). An important input for nozzle flow moving needle simulations is the needle lift profile which was extracted from the images [31, 32, 33].

3. Modelling approach

The simulations are computed using the commercial CFD code ANSYS Fluent [53]. The nozzle flow is solved using a homogeneous, three-phase mixture model (liquid fuel, vapour fuel and air) where all phases share the same velocity, pressure and temperature. The code is supplemented with user defined functions (UDFs) for implementation of the thermo-hydraulic properties of diesel and the needle movement.

3.1. Multiphase model

The properties appearing in the transport equations are determined by the presence of the component phases in each control volume. Defining α_{liq}, α_{vap} , α_{air} as the volume fraction of liquid fuel, air and vapour fuel in a cell,

Figure 1: Experimental results. Time sequence of a pilot injection transparent nozzle tip visualisation.

respectively, the density in each cell is given by: $\rho = \alpha_{liq}\rho_{liq} + \alpha_{vap}\rho_{vap} + \alpha_{air}\rho_{air}$.

All other transport properties (viscosity and thermal conductivity) are computed in this manner despite the fact that for homogeneous mixtures it is not clear how one should average each phase's effect, whether based on mass, volume or area (which would require knowledge of interfacial surface-area density). Although in the case of bubbly flows some theoretical derivations attributed to Einstein do exist [54], viscosity in general depends non linearly on the void fraction and in order to achieve accurate pressure drop calculations the mixture viscosity has to be empirically corrected by fitting coefficients to match experimental data sets [55]. For a review on the available correlations for the transport properties the interested reader is referred to [56]. Obviously, the volume constraint $\alpha_{liq} + \alpha_{air} + \alpha_{vap} = 1$, in each cell must be respected. The solved equations consist of the continuity, momentum and energy of the mixture, and the mass conservation equations for the vapor and the air:

$$\frac{\partial \rho}{\partial t} + \nabla \cdot (\rho \boldsymbol{v}) = 0 \tag{1}$$

$$\frac{\partial \rho \boldsymbol{v}}{\partial t} + \nabla \cdot (\rho \boldsymbol{v}\boldsymbol{v}) = -\nabla p + \nabla \cdot \sigma \tag{2}$$

$$\frac{\partial \rho E}{\partial t} + \nabla \cdot (\boldsymbol{v}(\rho E + p)) = \nabla \cdot (k_{eff} \nabla T) + \sigma \cdot \boldsymbol{v} \tag{3}$$

$$\frac{\partial \alpha_{vap}\rho_{vap}}{\partial t} + \nabla \cdot (\alpha_{vap}\rho_{vap}\boldsymbol{v}) = R_e - R_c \tag{4}$$

$$\frac{\partial \alpha_{air}\rho_{air}}{\partial t} + \nabla \cdot (\alpha_{air}\rho_{air}\boldsymbol{v}) = 0 \tag{5}$$

The source terms R_e and R_c represent the mass transfer between liquid and vapour phase due to cavitation. The effective viscous stress tensor is defined as $\sigma = \tau + \tau_t = \mu(\nabla v + (\nabla v)^T) + \tau_t$,

where μ is the viscosity of the mixture and τ_t are the turbulent stresses defined per the turbulence model being used. The energy is computed as the mass average for each phase and the internal energy of each phase is based on the local thermodynamic conditions of that phase [37].

The source terms appearing in the vapour volume fraction transport equation $(R_e - R_c)$ represent the mass transfer between fuel liquid and vapour phases due to cavitation bubble expansion and collapse respectively. The calculation of these values is based on the Rayleigh-Plesset equation describing bubble expansion and collapse [57], and its magnitude is based on the Zwart-Gerber-Belamri cavitation model [58] which reads as:

$$R_e = F_{vap}\frac{(3\alpha_{nuc}(1-\alpha_{vap})\rho_{vap})}{R_b}\sqrt{\frac{2}{3}\frac{max((p_{vap}-p),0)}{\rho_{liq}}} \tag{6}$$

$$R_c = F_{cond}\frac{(3\alpha_{vap}\rho_{vap})}{R_b}\sqrt{\frac{2}{3}\frac{max((p-p_{vap}),0)}{\rho_{liq}}} \tag{7}$$

F_{vap} and F_{cond} are empirical calibration coefficients, α_{nuc} is the volume fraction associated with the nuclei contained in the liquid and R_b the assumed bubble radius and p_{vap} is the vapour pressure. According to [58], values of $R_b = 10^{-6}m$, $\alpha_{nuc} = 5 \times 10^{-4}$, $F_{vap} = 50$, $F_{cond} = 0.01$ give reasonable results in a wide range of flows. Nevertheless, as discussed in [59] the mass transfer magnitude for these values could be insufficient creating areas of unrealistic liquid tension and not reproducing correctly the Rayleigh-Plesset bubble collapse, the suggested solution is to increase the empirical calibration coefficients several orders of magnitude to approximate the model to a Homogeneous Equilibrium Model (HEM). However, within this work the original coefficients published in[58]were used.

3.2. Turbulence model

The target when using LES is to capture the large scales that are dependent of the physical domain simulated while modelling the sub-grid turbulent scales. This is achieved by filtering of the Navier-Stokes equations using a spatial low-pass filter determined by the cell size of the computational domain used. This operation leaves the flow equations unchanged, but transforms the equations into equations for the filtered magnitudes [60]. During this operation terms in the equations appear representing the sub grid scale contributions to the equations of motions and have to be modelled. The closure of the model requires calculating a suitable sub grid turbulent dissipation (viscosity) μ_t. For such purpose, the Wall-Adapting Local Eddy-Viscosity

(WALE) model is chosen [61]. This model is capable of correctly reproducing the correct turbulence wall behaviour ($\mu_t \sim o(y^3)$) and becomes 0 at $y = 0$, being y the normal distance to the wall. Another advantage is that it returns a zero turbulent viscosity for laminar shear flows which allows the correct treatment of laminar zones in the domain, this is necessary for modelling the start of injection when flow velocities are low.

3.3. Fluid properties

High injection pressures and low lifts cause high injection velocities and transient heating effects making an incompressible approach unjustifiable [36, 37, 35]. Even if for the transparent nozzle tip testing conditions the pressure is lower than engine conditions, the diesel liquid phase is modelled as a compressible liquid based on the measurements made for the calibration oil Normafluid ISO4113. This is the usual fuel for testing and calibrating diesel fuel injection systems in both laboratories and at an industrial level. All diesel properties that follow are taken from [62, 63], where details of the measurement methodology, range of validity, method for fitting the coefficients and their values can be found (see Figure 2 for plots of the density and viscosity values for different pressures and temperatures). These properties were implemented into ANSYS Fluent following the available User-Defined-Real-Gas-Model (UDRGM) functionality as in [37]. As mentioned in the experimental results section, air compressibility effects are observed during the sac filling event and therefore the air density is modelled as an ideal gas

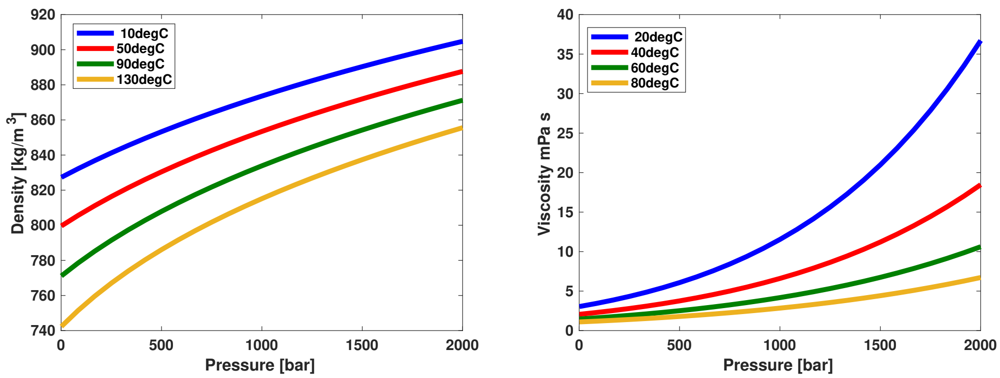

Figure 2: Diesel fuel properties implemented. Density (left) and viscosity (right) diesel fuel properties used.

with equation of state $p = \rho RT$.

3.4. Moving mesh methodology. Mesh generation and boundary conditions.

Modelling the dynamic movement of the needle is inherently difficult. At low lifts the cells in the seat are squeezed into very small gaps deteriorating their quality, which can have an impact on the robustness and accuracy of the simulation. Moreover, the contact between walls is not trivial to model since the continuity of the mesh is broken. Recent advances have been reported in [50] where the immersed boundary method has allowed simulations to be performed even at zero needle lift; however, this method has not been adopted here and as a compromise, the closed needle is modelled using the seat surface as a wall when the needle lift is below $1\mu m$.

The approach followed is based on an interpolation approach between two topologically identical meshes (key-grids) with the same number of cells and was already employed by the authors in [64]. The initial mesh has a $1\mu m$

lift and the high lift mesh is based on the maximum lift reached for the pilot injection $36 \mu m$. Based on the node position of this two meshes any intermediate lift is achieved by linear interpolation between the node position of the two key-grids. Another difficulty associated is the loss of resolution in the seat passage as the needle reaches high lifts, this requires interpolating the results into another pair of key-grids such as in [37]. For the pilot injection cases considered here, this was not needed due to the relatively low lift attained ($36 \mu m$). Moreover, in order to save computational resources, just a 60^o sector is model (one hole) based on the nominal (target) geometry. Figure 3 (left) shows the computational domain, consisting of different surfaces; the hole, housing, needle, seat inlet and side surfaces. Additionally, a 2mm long conical discharge volume is added in order to move away the outlet boundary condition from the areas of interest. The computational mesh used for the LES flow simulation is a fully hexahedral mesh.

The LES settings are adapted from the basis of the previous successful studies on diesel [39, 40, 41, 42] and gasoline [64, 65] direct injection and primary breakup simulations. In order to choose the appropriate filter/mesh size for the LES, the Taylor micro-scales (λ_g) have been estimated. This length scale is the intermediate length scale at which fluid viscosity significantly affects the dynamics of turbulent eddies in the flow [66]. For the flow inside the transparent tip, the Reynolds number based on the nozzle hole diameter, outlet pressure and inlet temperature can be estimated to be $Re = \frac{(\rho V D)}{\mu} \sim 13000$. The Taylor micro-scales can then be approximated by

[60]: $\lambda_g = \sqrt{\frac{10D}{Re}} = 4.4\mu m$. However, in order to resolve the smallest eddies close to the wall, the non-dimensional wall distance based on the friction velocity has to be of the order of 1 ($y^+ \sim 1$) [60]. Therefore, additional refinement close to the walls is needed. An estimate of this value based on the turbulent boundary layer theory yields a cell wall distance of $\sim 0.2\mu m$. In order to reach a value of $\sim 5\mu m$ in the bulk flow without increasing excessively the number of cells, a cell growth ratio of 1.1 was applied in the wall. Under these constraints, a $\sim 5M$ element mesh was produced, with a volume change between neighbouring cells below 3, minimum cell angle of 27^o and $3D$ determinant (normalized triple product of the vectors starting from each cell node) above 0.6 for both key-grids. Special care was taken to refine the needle seat area in the stream-wise direction in order not to exceed for low lifts aspect ratios of 100 in the direction of the bulk flow. Figure 3 (right) depicts the two meshes needed for the interpolation method, and a front view of the mesh showing the additional refinement in the seat area. A pressure boundary conditions was applied to the inlet of the domain. The pressure at the injector entrance in the high-pressure pipe was taken from the experimentally recorded values for every individual injection event. During the opening phase, pressure decreases at the injector entrance due to the increasing flow through it. At the end of the injection an over pressure is observed due to the water hammer effect after needle closing. The pressure at the entrance of the injector was provided in [31]. A temperature of $300K$ was chosen for the flow entering the domain and an air mass fraction value

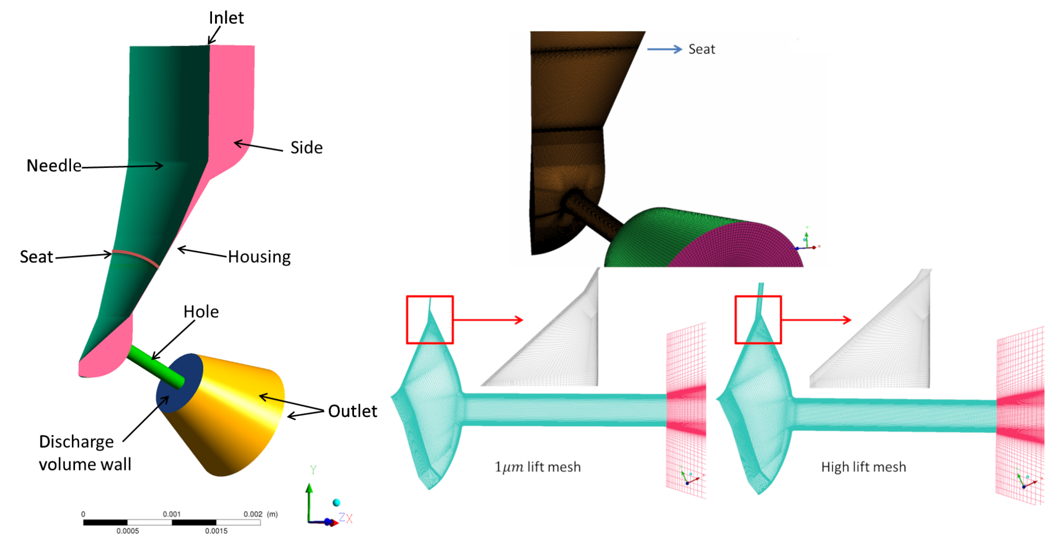

Figure 3: Geometrical model and mesh. Domain simulated and boundary conditions (left). Mesh showing seat refinement (right-top) and mesh cross section for both high and low lift meshes (right-bottom).

of 2×10^{-5} was imposed to take into account the possible dissolved air since it is a typical value for fuel or water exposed to ambient pressure [67]. The non-slip boundary conditions was applied to the non-moving wall (housing, hole, discharge volume wall, and, seat surface below $0.1\mu m$) as well as to the needle according to the motion profile resulting from the needle lift profile extracted from the images [31]. Periodic boundary condition have been applied to the side surfaces. Finally, a fixed pressure outlet was applied to the outlet surfaces, with pressure $1bar$ and $300K$ and air volume fraction prescribed as 1 in the case of back-flow.

The experimental images of the transparent nozzle show trapped air bubbles inside the injector before the start of injection. The mechanism behind

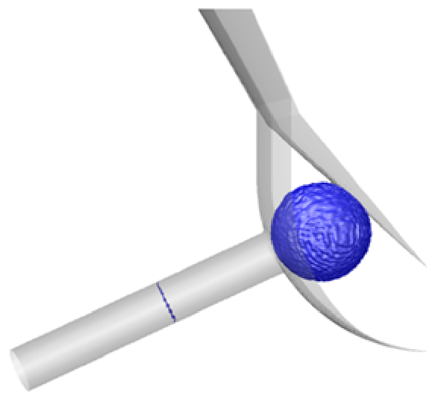

Figure 4: Initial simulation instant. Iso-surface of 0.5 liquid volume fraction and a mid-plane for the initial instant.

the appearance of this bubble is not straight forward to derive from the experimental images. Regardless, the LES nozzle flow simulation is initialised in qualitatively similar way; half of the hole is filled with air and an air spherical bubble is included in the sac (see Figure 4).

The computational domain above the seat surface is initialised at the pressure corresponding to that instant. Below the needle seat, the simulation is initialised at a pressure of $1bar$. All the domain is initialised at a temperature of $300K$ and with zero velocity. For the closing phase the movement of the needle is stopped when it reaches $1\mu m$ however the seat surface is not switched from interior to wall until the needle lift profile reaches $0.1\mu m$.

The solver used is segregated and pressure-based. The pressure-velocity coupling is achieved using the SIMPLEC algorithm [68]. Density is interpolated using a second order upwind scheme [69] while for the momentum a bounded central differencing scheme based on the normalized variable diagram (NVD) approach together with the convection boundedness criterion (CBC) [70] was used. The bounded central differencing scheme is a composite NVD-scheme that consists of a pure central differencing, a blended scheme of the central differencing and the second-order upwind scheme, and the first-order upwind scheme. The first-order scheme is used only when the CBC is violated. This scheme has small numerical dissipation and sufficient numerical stability for industrial LES simulations [71]. Among the volume fraction interpolation schemes available in ANSYS Fluent when using the mixture model, the quadratic upstream interpolation for convective kinetics (QUICK) scheme is selected in order to reduce the smearing of sharp volume fraction gradients and capture high density ratios [72]. Pressure interpolation follows the body force weighted scheme [53] and the temperature the first order upwind scheme. Finally the calculation of gradients was done using the Least Squares Cell-Based method.

The used solver is pressure-based and therefore the simulation stability is not limited by the acoustic wave propagation time scale. However, temporal resolution for LES requires minimum diffusion for the advection of the turbulent eddies. Therefore, an adaptive time step method is employed to ensure the advection CFL number stays below 1 throughout the computational domain.

3.5. LES mesh quality evaluation

The instantaneous fields of the LES quality metric of by Celik et al.[73] and y^+ for a representative moment at the highest lift ($t = 0.608ms$) are shown in Figure 5. Based on the y^+ the boundary layer resolution can be assessed; this value only exceeded 1 in areas above the seat and gradually transitions to values well under 1 ensuring a good wall shear resolution for the small eddies near the walls. Following [60] a good LES requires the modelled turbulent kinetic energy (k_{sgs}) to be less than 20 of the total turbulent energy ($k_{sgs} + k_{res}$), that is $\frac{k_{sgs}}{k_{sgs}+k_{res}} < 0.2$. However, as mentioned in [43] knowledge of k_{res} in the case of a moving needle injection can only be gained by repeating the simulation multiple times which could not be afforded computationally. Although they are point indicative measures which are not particularly accurate for anisotropic turbulence, another option is to use metrics based on the turbulence resolution length scale such as the LSR metric; see for example [74] and its application by Battistoni et al. [43] to a moving needle injection, or the similar metric by Celik et al.[73]:

$$LESIQ_\nu = \frac{1}{1 + 0.05(\frac{\mu+\mu_t}{\mu})^{0.53}} \tag{8}$$

where μ_t is the sub-grid scale viscosity introduced by the WALE model. This is a number between 0 and 1 for which the constants are calibrated such that the index is perceived similar to the ratio of resolved to total turbulent kinetic energy i.e. the higher the value the better the resolution is (0.8

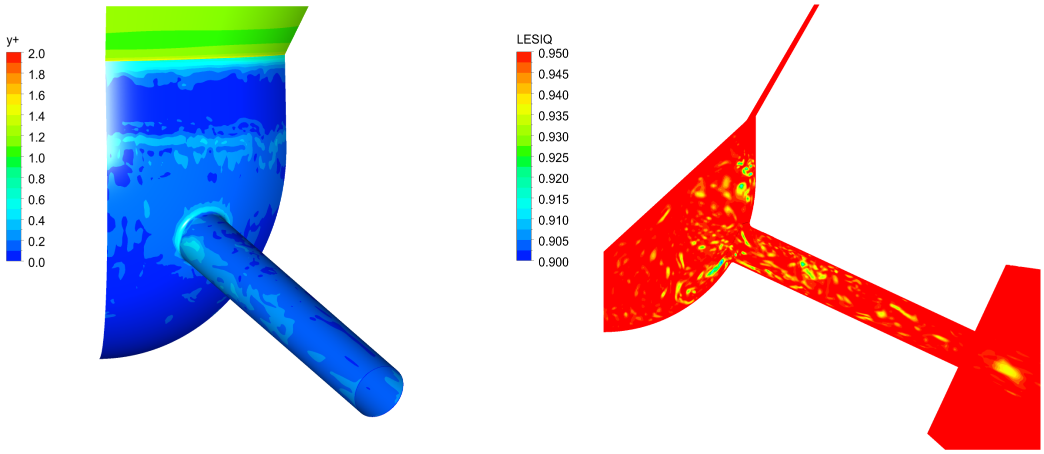

Figure 5: Mesh resolution evaluation. y^+ contours on the nozzle wall (left) and the LES quality metric of [73] (right) for highest needle lift during the pilot injection.

or above). Although [73] suggests to include as well the artificial visocsity introduced by the numerical methods, it is beyond the scope of this work to estimate such contribution. As seen in Figure 5 the value of $LESIQ_\nu$ for the same representative time instant is mostly over 0.95 throughout the domain and having a minimum values of 0.9 in the separation region that occurs at the entrance of the sac, confirming the suitability of the mesh.

4. Results and discussion

The evolution of the volume fraction inside the nozzle for the different phases is shown in Figure 6. Additionally, the imposed needle lift extracted from the image sequence shown in Figure 1 is shown as well. The simulation is started at the physical time $0.4874ms$ coincident with a lift of $1\mu m$ for the imposed profile. During the opening phase it follows from this plot that initially there is air present inside the nozzle. This air is evacuated out of

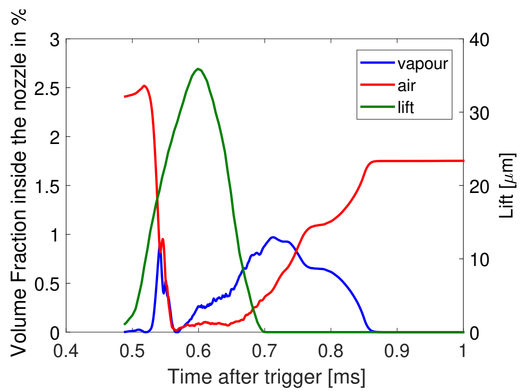

Figure 6: Integral results. Volume of vapour and air inside the nozzle and needle lift against time.

the nozzle while cavitation is generated showing a peak between $0.5ms$ and $0.6ms$, while it decreases afterwords. As the injection transitions towards the closing phase the amount of vapour increases, showing a peak just after the needle closes, while the amount of air continually increases by a process of air suction as it will be shown in the following section.

A comparison between the transparent nozzle tip images and the simulation results at the start of the injection is shown in Figure 7. In particular, a snapshot of the predicted liquid volume iso-surface of 50 at $t = 0.532ms$ is shown. At the early stages of the injection the simulation reproduces the compression of the air bubble inside the sac volume. The compression is caused by the pressure build up in the sac, justifying the inclusion of the compressibility of the air. This is quickly followed by cavitation originating at the needle seat passage, due to flow separation and shear in this area.

Sample simulation results and the transparent nozzle tip images for the needle opening phase are shown in Figure 8. The CFD results indicate that

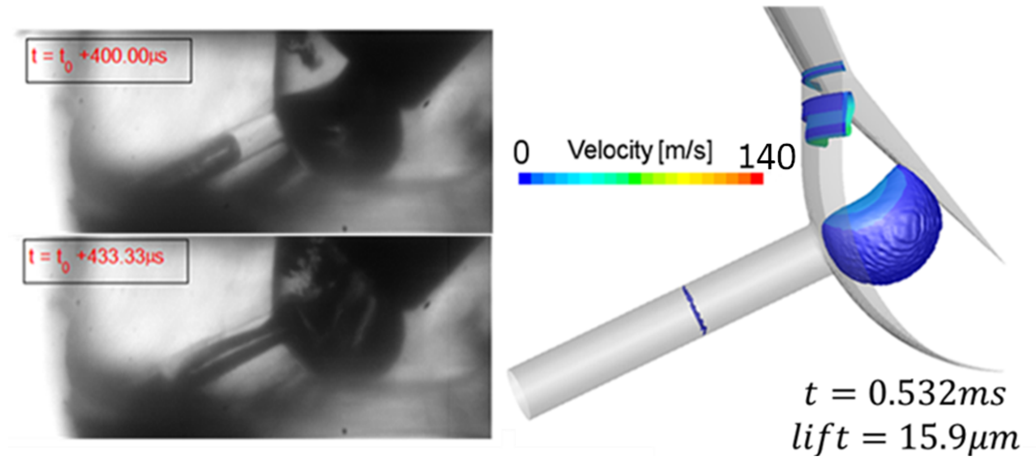

Figure 7: Start of injection results. Experimental visualisations (left), 50% liquid volume fraction iso-surface coloured by velocity magnitude (right).

cavitation produced at the sac entrance is transported directly into the injection hole. Simultaneously, the air bubble is further compressed and is pushed to recirculate parallel to the needle in the direction of the needle motion. Similarly to the experimental images, the air bubble is seen breaking down and mixing with any remaining cavitation into a fine bubbly mixture which is then advected into the hole.

As the needle lift increases and the flow further develops, the simulation indicates that air disappears from the sac volume, as seen in Figure 9. This is attributed to a combination of two effects. Firstly, the sac pressure build up causes the air to be compressed, reducing its volume fraction. Secondly, as the air is trapped within the recirculation zone developing inside the sac volume, it enters into the injection hole, where it expands due to the local pressure drop at its entrance. This contributes to the void areas observed

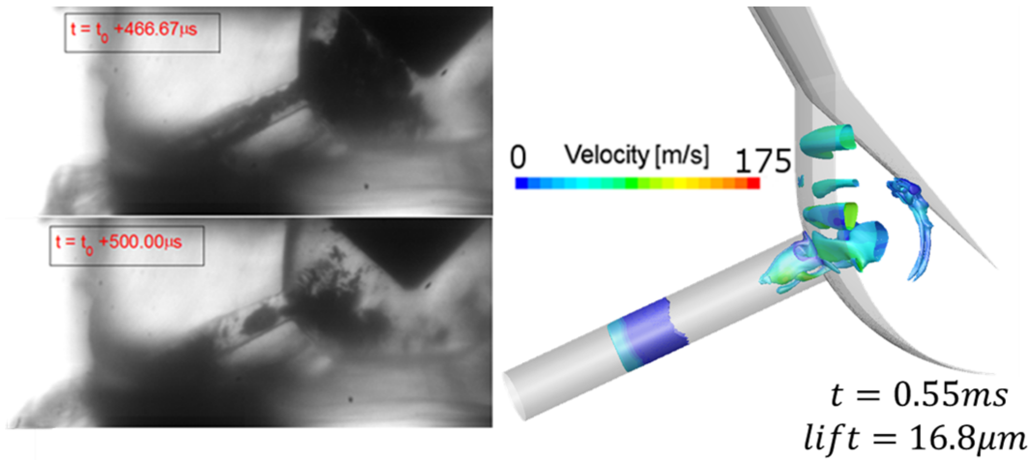

Figure 8: Needle opening phase results. Experimental visualisations (left), 50% liquid volume fraction iso-surface coloured by velocity magnitude (right).

and suggests that the void observed experimentally is a combination of air and fuel vapour. In addition, part of the void visible in the simulation can be attributed to geometrical cavitation developed at the hole inlet upper lip, which can be also seen from the experimental images.

The only two experimental frames available for the needle closing phase together with the simulation results are shown in Figure 10 (top). As the needle valve moves into the closing phase, the amount of void in the hole increases. This is in agreement with the simulation results from Figure 6, where volume content as a percentage of the injector volume of both air and vapour are plotted against time; it follows that these quantities increase during the needle closing phase. This void in the simulation has two sources, one from the unstable vortical flow developing inside the sac volume and entering into the injection hole and another due to formation of geometric-induced cavi-

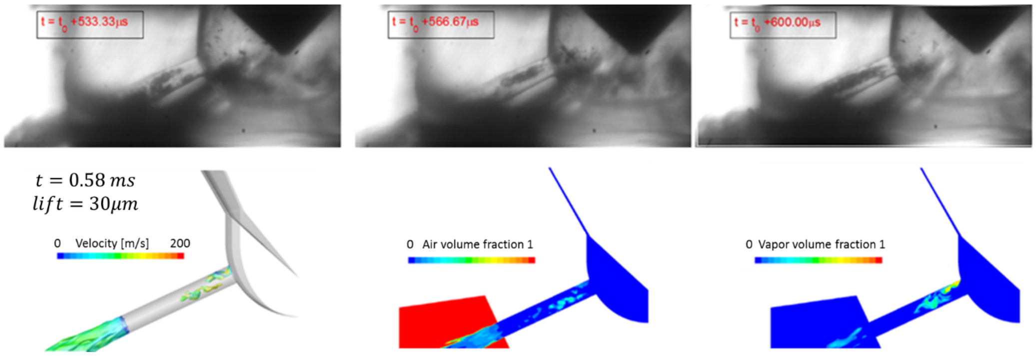

Figure 9: Results as flow further develops during the opening phase. Experimental visualisations for three time instances (top), 50% liquid volume fraction iso-surface coloured by velocity magnitude (bottom-left), air volume fraction contours (bottom-centre) and vapour volume fraction contours (bottom-right).

tation at the hole inlet corner. Regarding the experimental results at very low lifts ($lift = 6\mu m$), a bubbly mixture appears in the sac; bubbles having sizes similar to the hole diameter appear in the hole. The simulation model predicts high velocities in the hole; however, since the flow coming from the seat is throttled a void structure appears in front of the hole. The bubbly mixture in the sac volume correlates to the void structure created in front of the hole, which is predicted to be composed of a mixture of fuel vapour and expanded air. On the other hand, the visualised bubbles computed inside the injection hole correlate to the big amount of cavitation computed in the hole.

A time sequence of the pressure field is presented in Figure 11. Before the needle valve closes, the predicted sac volume pressure is still higher than the ambient pressure ($t = 0.674ms$), but immediately after the needle valve closing ($t = 0.698ms$), a pressure wave is generated that travels towards the

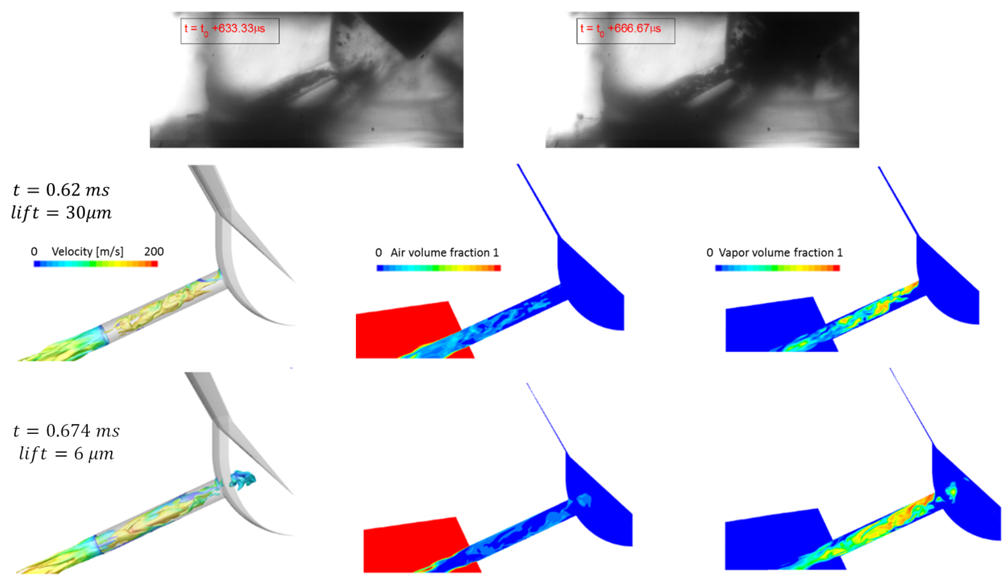

Figure 10: Needle closing results. Experimental visualisations for two time instants (top). Simulation results (center and bottom). For the simulation results 50% liquid volume fraction iso-surface coloured by velocity magnitude (left), air volume fraction contours (center) and vapour volume fraction contours (right) are presented.

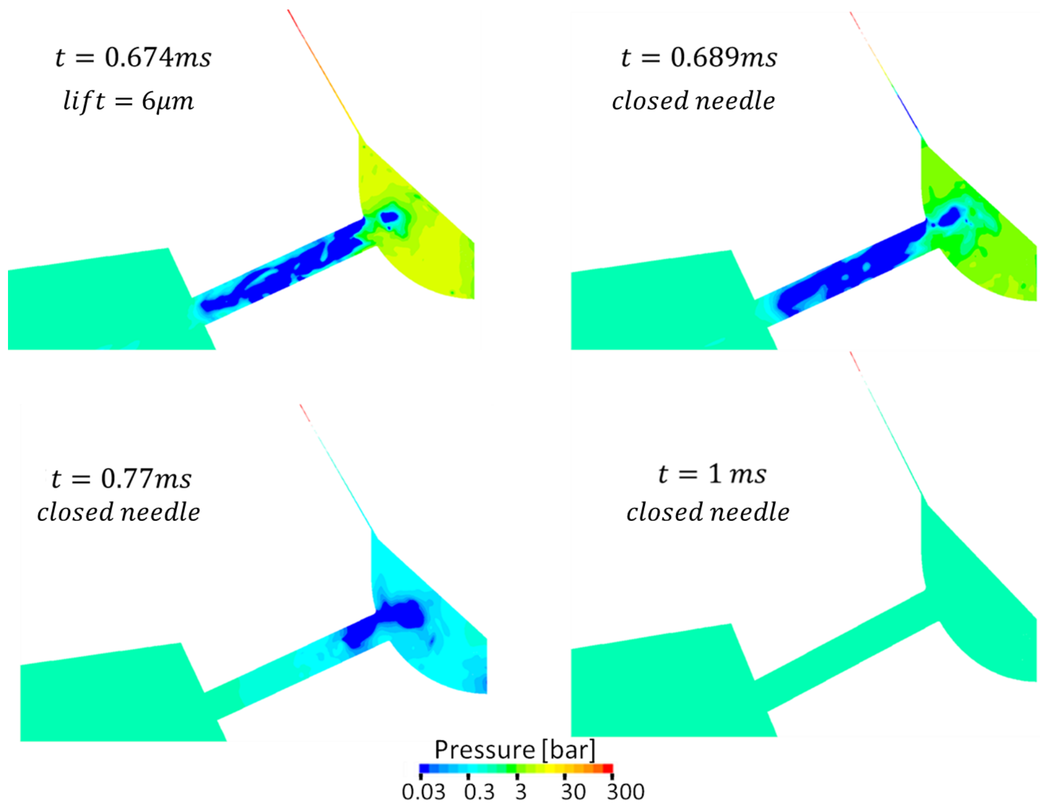

Figure 11: Pressure field time sequence. Notice that logarithmic scale has been used.

sac volume; this leaves the sac volume pressure below the ambient pressure ($t = 0.77ms$). In agreement with Figure 6, where air volume fraction inside the nozzle is seen to increase after needle closing, this induces the spray to weaken and air to be sucked back from the ambient into the nozzle until the sac pressure is balanced with the exterior pressure ($t = 1ms$).

Evidence is also provided in Figure 12, which shows a time sequence of air and vapour volume fraction fields. It clearly depicts the weakening flow momentum in the injection hole ($t = 0.698ms$) leading to air suction

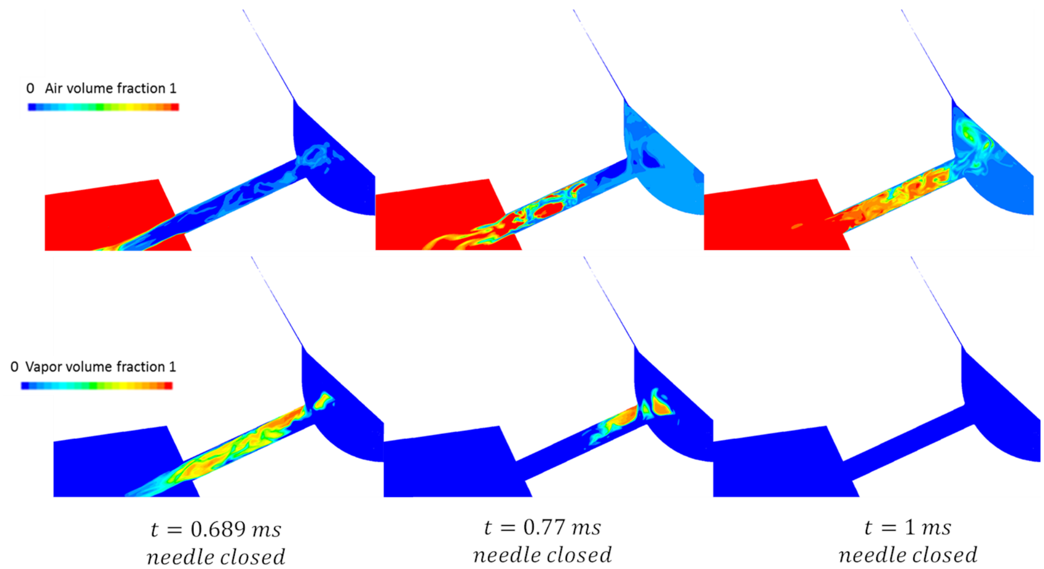

Figure 12: After needle closing results. Time sequence for air (top) and vapour (bottom) volume fraction fields.

($t = 77ms$). Finally, due to the pressure balancing with the ambient pressure, vapour completely disappears ($t = 1ms$), indicating that shortly after the needle closing only liquid and air remain inside the sac volume.

5. Conclusions

This paper presents an investigation of cavitation and air interaction during a diesel pilot injection of a standard serial production six-hole geometry. The focus was to understand the complex interaction between the needle motion, cavitation formation and development, and gas suction. The strategy followed has been to use high speed visualisations of a transparent nozzle tip to record the multiphase phenomena and to use CFD to explain the physics behind the observations. The CFD methodology includes LES turbulence modelling, the needle valve movement, cavitation effects through a Rayleigh-Plesset based cavitation model, and the compressibility of both air and fuel. Starting from a flow field initialised according to the experimental observations (with an air bubble in the sac and a big portion of the hole filled with air), the main flow features observed are replicated by the simulations. In particular the following phenomena experimentally noticed have been explained and reproduced:

- The compression of the initial air bubble due to sac pressure build up. The inclusion of air compressibility in the simulation can be very relevant even for modest injection pressures in order to replicate the air compression in the sac at the start of the injection as well as the air expansion in the injection hole and sac.

- The appearance of cavitation stemming from the sac entry at the start of the injection, due to flow separation and shear.

- The sac flow recirculation in the sac and flow patterns inside the hole. One part of the void observed in the simulation can be attributed to cavitation both geometrical (developed at the hole inlet upper lip) and vortical (due to complex flow structure coming from the sac). Furthermore, the initial air inside the nozzle expands in the hole contributing to the void areas observed. This shows that the void observed experimentally is a combination of both air and fuel vapour.

- An increase of void inside the hole and in the sac during the needle valve closing. The underlying reason being the flow throttling, since liquid momentum is still high but flow passage very restricted.

- The air suction after the needle closing. The closure of the valve creates an expansion wave that leaves the sac pressure below the ambient. This induces vapour creation and air expansion in the sac and consequently air is sucked from the ambient into the nozzle. When the pressure in the sac is recovered, all vapour collapses. Therefore, it is shown that the remaining foam at the end of the injection consists of a liquid and air mixture.

Acknowledgements

The European Union Horizon-2020 Research and Innovation Program funding to Eduardo Gomez Santos (No 675676), the ANSYS HPC research license grant to Delphi Technologies, and the CPU time granted by Gompute are highly appreciated.

References

[1] European-Comission, “Commission regulation (eu) 2017/1151 of 1 june 2017,” July 2017. `https://eur-lex.europa.eu/legal-content/EN/TXT/?uri=CELEX:02017R1151-20190101`. Last accessed 18th November 2019.

[2] S. Shundoh, M. Komori, K. Tsujimura, and S. Kobayashi, “Nox reduction from diesel combustion using pilot injection with high pressure fuel injection,” in *SAE Technical Paper*, SAE International, 1992. https://doi.org/10.4271/920461.

[3] D. A. Pierpont, D. T. Montgomery, and R. D. Reitz, “Reducing particulate and nox using multiple injections and egr in a d.i. diesel,” in *SAE Technical Paper*, SAE International, 1995. https://doi.org/10.4271/950217.

[4] H. Afzal, C. Arcoumanis, M. Gavaises, and N. Kampanis, “Internal flow in diesel injector nozzles modelling and experiments,” in *Fuel injection systems. Proceedings*, 1999. https://doi.org/10.1016/j.fuel.2013.08.060.

[5] E. Giannadakis, M. Gavaises, and C. Arcoumanis, “Modelling of cavitation in diesel injector nozzles,” *Journal of Fluid Mechanics*, vol. 616, pp. 153–193, 2008. https://doi.org/10.1017/S0022112008003777.

[6] I. H. Sezal, S. J. Schmidt, G. H. Schnerr, M. Thalhamer, and M. Förster, “Shock and wave dynamics in cavitating compressible liquid flows in injection nozzles,” *Shock Waves*, vol. 19, pp. 49–58, Apr 2009. https://doi.org/10.1007/s00193-008-0185-3.

[7] F. Salvador, J.-V. Romero, M.-D. Rosello, and J. Martinez-Lopez, “Validation of a code for modeling cavitation phenomena in diesel injector

nozzles," *Mathematical and Computer Modelling*, vol. 52, no. 7, pp. 1123 – 1132, 2010. `https://doi.org/10.1016/j.mcm.2010.02.027`.

[8] M. Ikemoto, K. Shimode, K. Omae, and N.Toda, "Diesel spray and combustion development using nozzle flow visualization , spray and combustion analyses," in *Proceedings of International Congress : SIA Powertrain -Rouen*, 2016.

[9] S. Moon, W. Huang, Z. Li, and J. Wang, "End-of-injection fuel dribble of multi-hole diesel injector: Comprehensive investigation of phenomenon and discussion on control strategy," *Applied Energy*, vol. 179, pp. 7 – 16, 2016. `https://doi.org/10.1016/j.apenergy.2016.06.116`.

[10] H. Kyu Suh and C. Sik Lee, "Effect of cavitation in nozzle orifice on the diesel fuel atomization characteristics," *International Journal of Heat and Fluid Flow*, vol. 29, pp. 1001–1009, 08 2008. `https://doi.org/10.1016/j.ijheatfluidflow.2008.03.014`.

[11] R. Miranda, H. Chaves, U. Martin, and F. Obermeier, "Cavitation in a transparent real size vco injection nozzle," in *Proceedings of the 9th International conference on liquid atomisation and spray systems, ICLASS, Sorrento*, 2003.

[12] I. Gilles-Birth, M. Rechs, U. Spicher, and S. Bernhardt, "Experimental investigation of the in-nozzle flow of valve covered orifice nozzles for

gasoline direct injection," in *Proceedings of the 7th International symposium on internal combustion diagnostics, Baden-Baden*, 2006.

[13] C. Arcoumanis, H. Flora, M. Gavaises, and M. Badami, "Cavitation in real-size multi-hole diesel injector nozzles," in *SAE 2000 World Congress*, SAE International, mar 2000. https://doi.org/10.4271/2000-01-1249.

[14] C. Arcoumanis, M. Gavaises, H. Flora, and H. Roth, "Visualisation of cavitation in diesel engine injectors," *Mecanique & Industries*, vol. 2, no. 5, pp. 375 – 381, 2001. http://www.sciencedirect.com/science/article/pii/S1296213901011198.

[15] H. Roth, E. Giannadakis, M. Gavaises, C. Arcoumanis, K. Omae, I. Sakata, M. Nakamura, and H. Yanagihara, "Effect of multi-injection strategy on cavitation development in diesel injector nozzle holes," in *SAE 2005 World Congress & Exhibition*, SAE International, apr 2005. https://doi.org/10.4271/2005-01-1237.

[16] C. Arcoumanis, M. Gavaises, E. Abdul-Wahab, and V. Moser, "Modeling of advanced high-pressure fuel injection systems for passenger car diesel engines," in *International Congress & Exposition*, SAE International, mar 1999. https://doi.org/10.4271/1999-01-0910.

[17] N. Mitroglou and M. Gavaises, "Cavitation inside real-size fully transparent fuel injector nozzles and its effect on near-nozzle spray forma-

tion," in *DIPSI workshop on droplet impact phenomena and spray investigations, University of Bergamo, Italy*, 2011.

[18] H. Chaves, R. Miranda, and R. Knake, "Particle image velocimetry measurements of the cavitating flow in a real size transparent vco nozzle," in *Proceedings of the 22nd European conference on liquid atomization and spray systems, ILASS, Como*, 2008. `https://doi.org/10.1017/jfm.2013.32`.

[19] A. Andriotis, M. Gavaises, and C. Arcoumanis, "Vortex flow and cavitation in diesel injector nozzles," *Journal of Fluid Mechanics*, vol. 610, pp. 195–215, 2008. `https://doi.org/10.1017/S0022112008002668`.

[20] G. Sridhar and J. Katz, "Effect of entrained bubbles on the structure of vortex rings," *Journal of Fluid Mechanics*, vol. 397, pp. 171–202, 1999. `https://doi.org/10.1017/S0022112099006187`.

[21] A. J. Cihonski, J. R. Finn, and S. V. Apte, "Volume displacement effects during bubble entrainment in a travelling vortex ring," *Journal of Fluid Mechanics*, vol. 721, pp. 225–267, 2013.

[22] J. Choi and S. L. Ceccio, "Dynamics and noise emission of vortex cavitation bubbles," *Journal of Fluid Mechanics*, vol. 575, pp. 1–26, 2007. `https://doi.org/10.1017/S0022112006003776`.

[23] J. Choi, C.-T. Hsiao, G. Chahine, and S. Ceccio, "Growth, oscillation and collapse of vortex cavitation bubbles," *Journal of Fluid Me-*

chanics, vol. 624, pp. 255–279, 2009. https://doi.org/10.1017/S0022112008005430.

[24] S. Dabiri, W. A. Sirignano, and D. D. Joseph, "Interaction between a cavitation bubble and shear flow," *Journal of Fluid Mechanics*, vol. 651, pp. 93–116, 2010. https://doi.org/10.1017/S0022112009994058.

[25] M. Blessing, G. Konig, C. Kruger, U. Michels, and V. Schwarz, "Analysis of flow and cavitation phenomena in diesel injection nozzles and its effects on spray and mixture formation," in *SAE 2003 World Congress & Exhibition*, SAE International, mar 2003. https://doi.org/10.4271/2003-01-1358.

[26] M. Gavaises, D. Papoulias, A. Andriotis, E. Giannadakis, and A. Theodorakakos, "Link between cavitation development and erosion damage in diesel injector nozzles," in *SAE World Congress & Exhibition*, SAE International, apr 2007. https://doi.org/10.4271/2007-01-0246.

[27] B. Reid, G. Hargrave, C. P. Garner, and G. Wigley, "An investigation of string cavitation in a true-scale fuel injector flow geometry at high pressure," *Physics of Fluids*, vol. 22, 03 2010. https://doi.org/10.1063/1.3372174.

[28] M. Gavaises, B. Reid, N. Mitroglou, G. Hargrave, C. Garner, E. Long, and R. Mcdavid, "On the formation of string cavitation inside fuel in-

jectors," *Experiments in Fluids*, vol. 55, 01 2014. https://doi.org/10.1007/s00348-013-1662-8.

[29] R. Lockett and A. Bonifacio, "Hydrodynamic luminescence in a model diesel injector return valve," *International Journal of Engine Research*, 07 2019. https://doi.org/10.1177/1468087419870421.

[30] L. Thimm, P. Trtik, H. Hansen, S. Jollet, and F. Dinkelacker, "Experimental cavitation and spray measurement in real size diesel injection nozzles with high resolution neutron imaging," in *Proceedings of the 29th Conference on Liquid Atomization and Spray Systems, ILASS Europe, Paris*, 2019.

[31] M. McLorn, *Fundamental Behaviour of Valves Used in Diesel Fuel Injection Equipment*. PhD thesis, (Unpublished), City, University of London, 2013.

[32] N. Mitroglou, M. McLorn, M. Gavaises, C. Soteriou, and M. Winterbourne, "Instantaneous and ensemble average cavitation structures in diesel micro-channel flow orifices," *Fuel*, vol. 116, pp. 736 – 742, 2014. https://doi.org/10.1016/j.fuel.2013.08.060.

[33] M. Winterbourn, C. Soteriou, N. Mitroglou, M. Gavaises, and C. Daveau, "Visualising injection events in a fully operational diesel injector with a multi-hole transparent tip," in *Thiesel, Valencia*, 2014.

[34] R. P. Fitzgerald, G. D. Vecchia, J. E. Peraza, and G. C. Martin, "Features of internal flow and spray for a multi-hole transparent diesel fuel injector tip," in *29th Conference on Liquid Atomization and Spray Systems, ILASS, Paris*, 2019.

[35] P. Koukouvinis, M. Gavaises, J. Li, and L. Wang, "Large eddy simulation of diesel injector including cavitation effects and correlation to erosion damage," *Fuel*, vol. 175, pp. 26 – 39, 2016. https://doi.org/10.1016/j.fuel.2016.02.037.

[36] A. Theodorakakos, G. Strotos, N. Mitroglou, C. Atkin, and M. Gavaises, "Friction-induced heating in nozzle hole micro-channels under extreme fuel pressurisation," *Fuel*, vol. 123, pp. 143 – 150, 2014. https://doi.org/10.1016/j.fuel.2014.01.050.

[37] G. Strotos, P. Koukouvinis, A. Theodorakakos, M. Gavaises, and G. Bergeles, "Transient heating effects in high pressure diesel injector nozzles," *International Journal of Heat and Fluid Flow*, vol. 51, pp. 257 – 267, 2015. https://doi.org/10.1016/j.ijheatfluidflow.2014.10.010.

[38] J. Shi, N. Guerrassi, G. Dober, K. Karimi, and Y. Meslem, "Complex physics modelling of diesel injector nozzle flow and spray supported by new experiments," in *Thiesel, Valencia*, 2014.

[39] J. Shi, P. Aguado Lopez, G. Dober, N. Guerrassi, W. Bauer, and M. Lai,

"Using les and x-ray imaging to understand the influence of injection hole geometry on diesel spray formation," in *Thiesel, Valencia*, 2016.

[40] J. Shi, P. Aguado Lopez, E. Gomez Santos, N. Guerrassi, G. Dober, W. Bauer, M. Lai, and J. Wang, "Evidence of vortex driven primary breakup in high pressure fuel injection," in *Proceedings of the 28th Conference on Liquid Atomization and Spray Systems, ILASS Europe, Valencia*, 2017. http://dx.doi.org/10.4995/ILASS2017.2017.5707.

[41] J. Shi, P. Aguado Lopez, N. Guerrassi, and G. Dober, "Understanding high-pressure injection primary breakup by using large eddy simulation and x-ray spray imaging," *MTZ worldwide*, vol. 78, pp. 50–57, 05 2017. https://doi.org/10.1007/s38313-017-0039-4.

[42] J. Shi, P. Aguado Lopez, E. Gomez Santos, N. Guerrasi, W. Bauer, M.-C. Lai, and J. Wang, "High pressure diesel spray development: the effect of nozzle geometry and flow vortex dynamics," in *Proceedings of the 14th International Conference on Liquid Atomization and Spray Systems, ICLASS, Chicago*, 2018.

[43] M. Battistoni, Q. Xue, and S. Som, "Large-eddy simulation (les) of spray transients: Start and end of injection phenomena," *Oil Gas Sci. Technol. - Rev. IFP Energies nouvelles*, vol. 71, no. 1, p. 4, 2016. https://doi.org/10.2516/ogst/2015024.

[44] S. Bornschlegel, C. Conrad, A. Durst, J. Wang, and M. Wensing, "Multi-

hole gasoline direct injection:in-nozzle flow and primary breakup investigated in transparent nozzlesand with x-ray," *International Journal of Engine Research*, vol. 19, no. 1, pp. 67–77, 2018. https://doi.org/10.1177/1468087417746860.

[45] F. Orley, S. Hickel, S. J. Schmidt, and N. A. Adams, "Large-eddy simulation of turbulent, cavitating fuel flow inside a 9-hole diesel injector including needle movement," *International Journal of Engine Research*, vol. 18, no. 3, pp. 195–211, 2017. https://doi.org/10.1177/1468087416643901.

[46] A. E. Catania, S. d'Ambrosio, R. Finesso, and E. Spessa, "Effects of rail pressure, pilot scheduling and egr rate on combustion and emissions in conventional and pcci diesel engines," *SAE Int. J. Engines*, vol. 3, pp. 773–787, 04 2010. https://doi.org/10.4271/2010-01-1109.

[47] S. Busch, K. Zha, P. C. Miles, A. Warey, F. Pesce, R. Peterson, and A. Vassallo, "Experimental and numerical investigations of close-coupled pilot injections to reduce combustion noise in a small-bore diesel engine," *SAE Int. J. Engines*, vol. 8, pp. 660–678, 04 2015. https://doi.org/10.4271/2015-01-0796.

[48] S. Busch, K. Zha, A. Warey, F. Pesce, and R. Peterson, "On the reduction of combustion noise by a close-coupled pilot injection in a small-bore direct-injection diesel engine," *Journal of Engineering for Gas Turbines and Power*, vol. 138, 04 2016. https://doi.org/10.1115/1.4032864.

[49] G. Dober, C. Garsi, N. Guerrassi, H. Ismail, and J. Shi, "Investigations of the spray structure of large and small diesel injections using spray momentum measurements and their link to injector performance," in *In Proceedings of SIA Powertrain Conference*, 06 2016.

[50] M. Gold, R. Pearson, J. Turner, D. Sykes, V. Stetsyuk, G. de Sercey, C. Crua, F. Koukouvinis, M. Gavaises, and M. Mithun, "Simulation and measurement of transient fluid phenomena within diesel injection," *SAE Int. J. Adv. & Curr. Prac. in Mobility*, vol. 1, pp. 291–305, 01 2019. https://doi.org/10.4271/2019-01-0066.

[51] H. Ismail, G. Dober, J. Shi, K. Karimi, and N. Guerrassi, "Delphi technologies internal report." 2016.

[52] G. Kalghatgi, *Fuel/Engine Interactions.* SAE International, 2013.

[53] *ANSYS Fluent Theory Guide*, 2018.

[54] D. Beattie and P. Whalley, "A simple two-phase frictional pressure drop calculation method," *International Journal of Multiphase Flow*, vol. 8, no. 1, pp. 83 – 87, 1982. https://doi.org/10.1016/0301-9322(82)90009-X.

[55] N. Aung and T. Yuwono, "Evaluation of mixture viscosity models in the prediction of two-phase flow pressure drops," *ASEAN Journal on Science and Technology for Development*, vol. 29, no. 2, 2012. https://doi.org/10.29037/ajstd.58.

[56] M. Awad and Y. Muzychka, "Effective property models for homogeneous two-phase flows," *Experimental Thermal and Fluid Science*, vol. 33, no. 1, pp. 106 – 113, 2008. https://doi.org/10.1016/j.expthermflusci.2008.07.006.

[57] C. Brennen, *Cavitation and bubble dynamics*. Oxford: Oxford University Press, 1995.

[58] P. J. Zwart, A. G. Gerber, and T. Belamri, "A two-phase flow model for predicting cavitation dynamics," in *Proceedings of the International Conference on Multiphase Flow, ICMF, Yokohama*, 2004.

[59] P. Koukouvinis, H. Naseri, and M. Gavaises, "Performance of turbulence and cavitation models in prediction of incipient and developed cavitation," *International Journal of Engine Research*, vol. 18, no. 4, pp. 333–350, 2017. https://doi.org/10.1177/1468087416658604.

[60] S. B. Pope, *Turbulent Flows*. Cambridge University Press, 2000.

[61] F. Nicoud and F. Ducros, "Subgrid-scale stress modelling based on the square of the velocity gradient tensor," *Flow, Turbulence and Combustion*, vol. 62, pp. 183–200, Sep 1999. https://doi.org/10.1023/A:1009995426001.

[62] E. H. I. Ndiaye, J.-P. Bazile, D. Nasri, C. Boned, and J. L. Daridon, "High pressure thermophysical characterization of fuel used for testing

and calibrating diesel injection systems," *Fuel*, vol. 98, pp. 288 – 294, 2012. https://doi.org/10.1016/j.fuel.2012.04.005.

[63] M. Chorazewski, F. Dergal, T. Sawaya, I. Mokbel, J.-P. E. Grolier, and J. Jose, "Thermophysical properties of normafluid (iso 4113) over wide pressure and temperature ranges," *Fuel*, vol. 105, pp. 440 – 450, 2013. https://doi.org/10.1016/j.fuel.2012.05.059.

[64] E. Gomez Santos, J. Shi, W. Bauer, and M. Gavaises, "Modelling and prediction of cavitation erosion in gasoline direct injection injectors operated with e100 fuel using a barotropic equation of state," in *Proceedings of the IMechE Fuel Systems Conference, London*, 2018.

[65] J. Shi, E. Gomez Santos, G. Hoffmann, and G. Dober, "Large eddy simulation as an effective tool for gdi nozzle development," *MTZ worldwide*, vol. 79, pp. 58–63, Oct. 2018. https://doi.org/10.1007/s38313-018-0089-2.

[66] H. Tennekes and J. Lumley, *A First Course in Turbulence*. MIT Press, 1972.

[67] M. Battistoni, S. Som, and D. Longman, "Comparison of mixture and multi-fluid models for in-nozzle cavitation prediction," in *Proceedings of ASME Internal Combustion Engine Division Fall Technical Conference, ICEF, Dearborn*, 10 2013.

[68] J. P. V. Doormaal and G. D. Raithby, “Enhancements of the simple method for predicting incompressible fluid flows,” *Numerical Heat Transfer*, vol. 7, no. 2, pp. 147–163, 1984. https://doi.org/10.1080/01495728408961817.

[69] J. Ferziger and M. Peric, *Computational Methods for Fluid Dynamics*. Springer Berlin Heidelberg, 2012.

[70] B. Leonard, “The ultimate conservative difference scheme applied to unsteady one-dimensional advection,” *Computer Methods in Applied Mechanics and Engineering*, vol. 88, no. 1, pp. 17 – 74, 1991. https://doi.org/10.1016/0045-7825(91)90232-U.

[71] F. R. Menter, “Best practice: scale-resolving simulations in ansys cfd,” in *ANSYS Technical report*, 2015.

[72] F. Moukalled, L. Mangani, and M. Darwish, *The Finite Volume Method in Computational Fluid Dynamics. An Advanced Introduction with OpenFOAM and Matlab*. Springer International Publishing, 1 ed., 2015. https://doi.org/10.1007/978-3-319-16874-6. Comparison of the QUICK and FOU schemes in pure advection of a step profile for a scalar ϕ in an oblique velocity field - pages 400 to 403.

[73] I. B. Celik, Z. N. Cehreli, and I. Yavuz, “Index of Resolution Quality for Large Eddy Simulations,” *Journal of Fluids Engineering*, vol. 127, pp. 949–958, 09 2005. https://doi.org/10.1115/1.1990201.

[74] F. Brusiani and G. M. Bianchi, “Les simulation of ice non-reactive flows in fixed grids,” in *SAE Technical Paper*, SAE International, 04 2008. https://doi.org/10.4271/2008-01-0959.